

Impacts of Hurricane Irma (2017) on ocean transport processes

Thomas Dobbelaere^{a,*}, Milan Curcic^b, Matthieu le Hénaff^{c,d}, Emmanuel Hanert^{a,e}

^a*Eath and Life Institute (ELI), UCLouvain, Louvain-la-Neuve, Belgium*

^b*Rosenstiel School of Marine and Atmospheric Sciences (RSMAS), University of Miami, Coral Gables, Florida, USA*

^c*Cooperative Institute for Marine and Atmospheric Studies (CIMAS), University of Miami, Miami, Florida, USA*

^d*Atlantic Oceanographic and Meteorological Laboratory (AOML), NOAA, Miami, Florida, USA*

^e*Institute of Mechanics, Materials and Civil Engineering (IMMC), UCLouvain, Louvain-la-Neuve, Belgium*

Abstract

Tropical cyclones are becoming more intense and more frequent. Their effect is particularly acute in coastal areas where they cause extensive damage leading to an influx of debris, sediments and waste to the sea. However, most coastal ocean models do not represent their transport correctly as they do not couple the hydrodynamics with the wind-generated waves. This may lead to significant errors in heavy-wind conditions. Here, we investigate current-wave interactions during a major cyclone and assess their impact on transport processes. We do that by coupling the unstructured-mesh coastal ocean model SLIM with the spectral wave model SWAN, and applying it to the Florida Reef Tract during Hurricane Irma (Sept. 17). We show that the coupled model successfully reproduces the wave behaviour, the storm surge and the ocean currents during the passage of the hurricane. We then use the coupled and uncoupled wave-current model to simulate the transport of

*Corresponding author

Email address: thomas.dobbelaere@uclouvain.be (Thomas Dobbelaere)

passive drifters. We show that the wave force alone can lead to changes of up to 1 m/s in the modelled currents, which in turn lead to differences of up to 10 km in the position of drifting material over the duration of the hurricane. [Add a sentence on Stokes drift vs wave-current coupling]. Our results suggest that wave-current interactions can strongly impact the transport of drifting material such as sediments and debris in the aftermath of a hurricane. They should thus be taken into account in order to correctly assess its overall impact

Keywords:

1. Introduction

2 Tropical cyclones are becoming more intense and more frequent (Bhatia
3 et al., 2019; Kossin et al., 2020). This increase is likely due to climate
4 change and will probably continue in the future (ref?). However, estimating
5 the impact of tropical cyclones on the coastal ocean circulation remains
6 a challenge. Understanding wave-current interactions and being able to
7 represent their impact on coastal ocean transport processes is central to many
8 coastal activities such as dredging, erosion management, O&G, search and
9 rescue (Bever and MacWilliams, 2013; Li and Johns, 1998; Breivik et al.,
10 2013). [Add 1/2 sentences]

11 Wave-current interactions during a cyclone are highly nonlinear and can
12 vary significantly in space and time (Wu et al., 2011). Wave-induced currents
13 are generated by wave radiation stress gradients (Longuet-Higgins, 1970), af-
14 fecting water levels near shorelines and wave breaking points (Longuet-Higgins
15 and Stewart, 1964). Changes in water levels and currents, in turn, affect the
16 motion and evolution of the waves (Sikirić et al., 2013). Coupled wave-current
17 models are therefore required to capture these complex interactions. [Add
18 1/2 sentences]

19 Coastal oceans are characterized by the complex topography of the coast-
20 line and the presence of islands, reefs and artificial structures. Traditional

21 structured-grid models often lack the flexibility to simulate near-shore pro-
22 cesses at a sufficiently small scale. Instead, unstructured-mesh models can
23 easily adapt to the topography and are hence better suited to coastal processes
24 (Wu et al., 2011; Chen et al., 2007) [Revoir ref]. Being able to capture the
25 impact of the topography on wave interactions becomes even more important
26 in the case of tropical cyclones. Heavy winds generate large wind-waves and
27 disturb ocean conditions (Liu et al., 2020) by causing coastal upwellings on
28 continental shelves (Smith, 1982) and inducing strong currents, waves and
29 storm surges in nearshore and coastal regions (Dietrich et al., 2010; Weisberg
30 and Zheng, 2006).

31 The transport of drifting objects or substances that are locally released
32 is often best represented by a Lagrangian individual-based model. Such
33 an approach is routinely used to model the dispersal of larvae, pollutants,
34 sediments and many other tracers (e.g. Le Hénaff et al. (2012); Liubartseva
35 et al. (2018); Figueiredo et al. (2013); Frys et al. (2020)). Although some
36 transport models take the impact of waves into account by adding a Stokes
37 drift velocity, *i.e.* the net drift of a floating particle in the direction of the wave
38 propagation (Van Den Bremer and Breivik, 2018), to the Eulerian currents,
39 they usually neglect the wave-induced currents. Such practice is reasonable
40 in the case of fair weather, when wave-induced forces exerted on currents are
41 relatively small, but might lead to significant errors during storm conditions
42 (Röhrs et al., 2012; Curcic et al., 2016).

43 The objective of this study is therefore to assess the importance of wave-
44 current interactions during a tropical cyclone. We investigate the transport
45 of drifting particles on the Florida shelf during Hurricane Irma, one of the
46 strongest and costliest tropical cyclones on record in the Atlantic Basin (Xian
47 et al., 2018), which made landfall in Florida in September 2017. To do that,
48 we developed an unstructured coupled wave-current model of South Florida to
49 simulate the ocean circulation during hurricane Irma. Both modelled currents
50 and waves were validated against field measurements and were then used to

51 simulate the transport of drifting material in the Florida Keys and the Florida
52 inner shelf. Model outputs were then compared with uncoupled simulation
53 results in order to assess the impact of wave-induced forces and Stokes drift
54 on the modelled currents and transports.

55 **2. Methods**

56 *2.1. Study area and observational data*

57 The large-scale ocean circulation around South Florida is dominated by
58 the Florida Current (FC), which originates from the Loop Current (LC) where
59 it enters the Florida Straits from the Gulf of Mexico, and, downstream, forms
60 the Gulf Stream. The FC is a major western boundary current characterized
61 by spatial variability and meandering, associated with the presence of cyclonic
62 eddies between the core of the current and the complex reef topography of
63 the Florida Reef Tract (FRT) (Lee et al., 1995; Kourafalou and Kang, 2012).
64 The variability of the FC extends over a large range of spatial and temporal
65 scales, with periods of 30-70 days in the Lower Keys (Lee et al., 1995) and
66 shorter periods of 2-21 days in the Upper Keys (Lee and Mayer, 1977), and
67 exhibits significant seasonal and interannual cycles (Johns and Schott, 1987;
68 Lee and Williams, 1988; Schott et al., 1988). Circulation on the West Florida
69 Shelf (WFS) on the other hand is forced by local winds and tidal fluctuations
70 (Lee and Smith, 2002; Liu and Weisberg, 2012). [Add sentences on tropical
71 cyclones in that area]

72 The state of the ocean around Florida is monitored by an extensive
73 array of tide gauges, current meters and buoys. In this study, we used sea
74 surface elevation measurements from the National Oceanic and Atmospheric
75 Administrations (NOAA) Tides and Currents dataset. These measurements
76 were taken at four locations: two in the Florida Keys (Key West and Vaca Key);
77 one on the eastern coast of Florida (Virginia Key); and one on the western
78 coast (Naples). For the currents, we used ADCP measurements from the
79 University of South Florida's College of Marine Science's (USF/CMS) Coastal

80 Ocean Monitoring and Prediction System (COMPS) for the WFS (Weisberg
81 et al., 2009). More specifically, we used measurements from moorings C10,
82 C12 and C13, respectively located at the 25, 50, and 50 m isobaths of the
83 WFS (Liu et al., 2020). Finally, for the waves, we used measurements from
84 four buoys of the NOAA's National Data Buoy Center (NDBC); two on
85 Florida's eastern shelf and two on the WFS. The locations of all measurement
86 stations are shown in Fig. 1A,C.

87 *2.2. Wind and atmospheric pressure during Hurricane Irma*

88 Irma made landfall in Florida on 10 September 2017 as a category 3
89 hurricane, first at Cudjoe Key (Florida Keys) and later on Marco Island,
90 south to Naples (see hurricane track in Fig. 1). It then weakened to a
91 category 2 hurricane as it moved further inland (Pinelli et al., 2018). The
92 storm damaged up to 75% of the buildings at its landfall point in the Florida
93 Keys, making it one of the strongest and costliest hurricanes on record in the
94 Atlantic basin (Xian et al., 2018; Zhang et al., 2019). The strongest reported
95 wind speed was 50 m/s on Marco Island while the highest recorded storm
96 surge was 2.3 m, although larger wind speed likely occurred in the Florida
97 Keys (Pinelli et al., 2018). In order to reproduce the wind profile of Irma in
98 our model, we used high-resolution H*Wind wind fields (Powell et al., 1998).
99 As these data represent 1-min averaged wind speeds, we multiplied them by a
100 factor 0.93 to obtain 10-min averaged wind speeds (Harper et al., 2010), which
101 are more consistent with the time step of our model. Furthermore, H*Wind
102 wind profiles did not cover the whole model extent during the passage of the
103 hurricane and were thus blended within coarser wind field extracted from
104 ECMWF ERA-5 datasets (Fig. 2A). The pressure field during the passage
105 of Hurricane Irma was also reconstructed using ERA-5 data. However, the
106 coarse resolution of the dataset smoothes out the depression at the center of
107 the hurricane, leading to an underestimation of the pressure gradient (Fig.
108 2B). To better capture the central depression of Irma, we therefore built a
109 hybrid pressure field using the position and the minimal pressure of the core

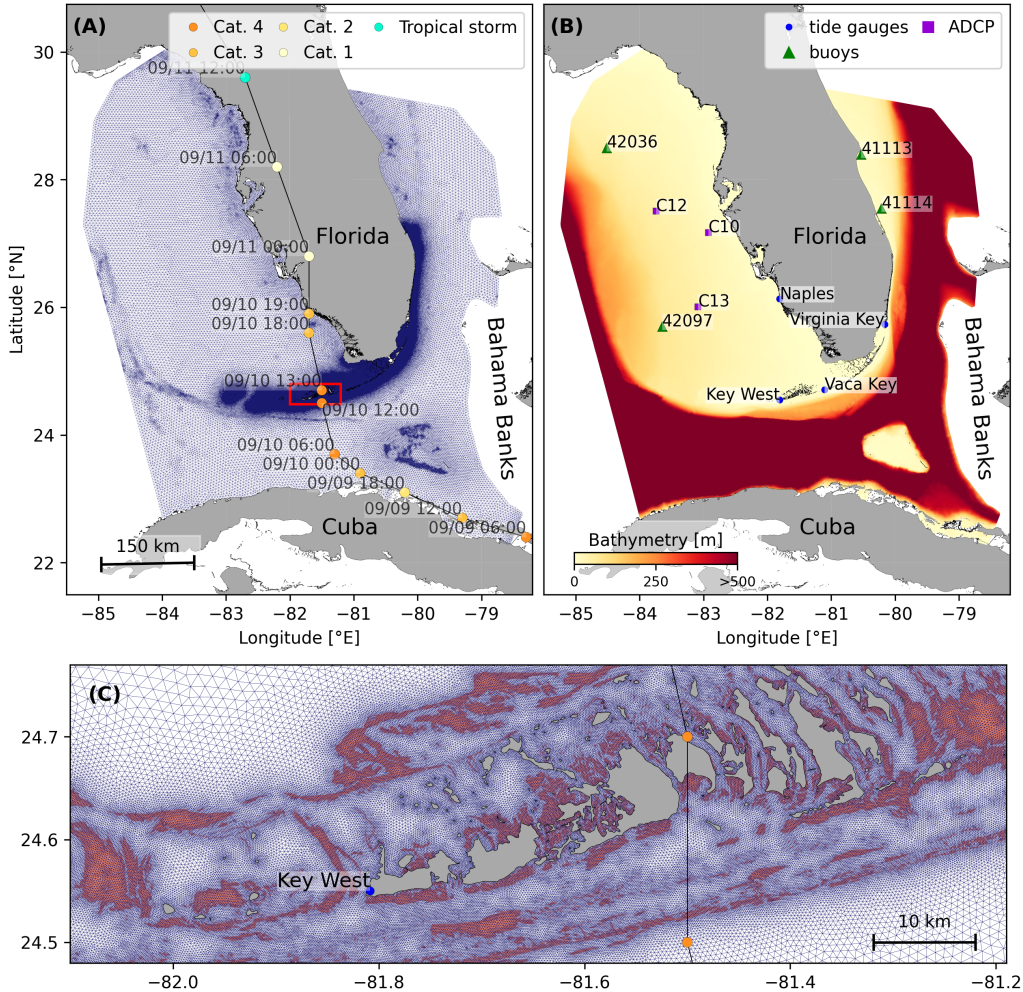


Fig. 1: (A) Mesh of the computational domain with the trajectory of Irma, category of the hurricane is given by the Saffir-Simpson color scale. (B) Bathymetry of the domain with the location of stations used for the validation of the model outputs. (C) Close up view of the Lower Keys area, where the mesh resolution reaches 100m near reefs (shown in dark orange) and islands (highlighted in dark grey)

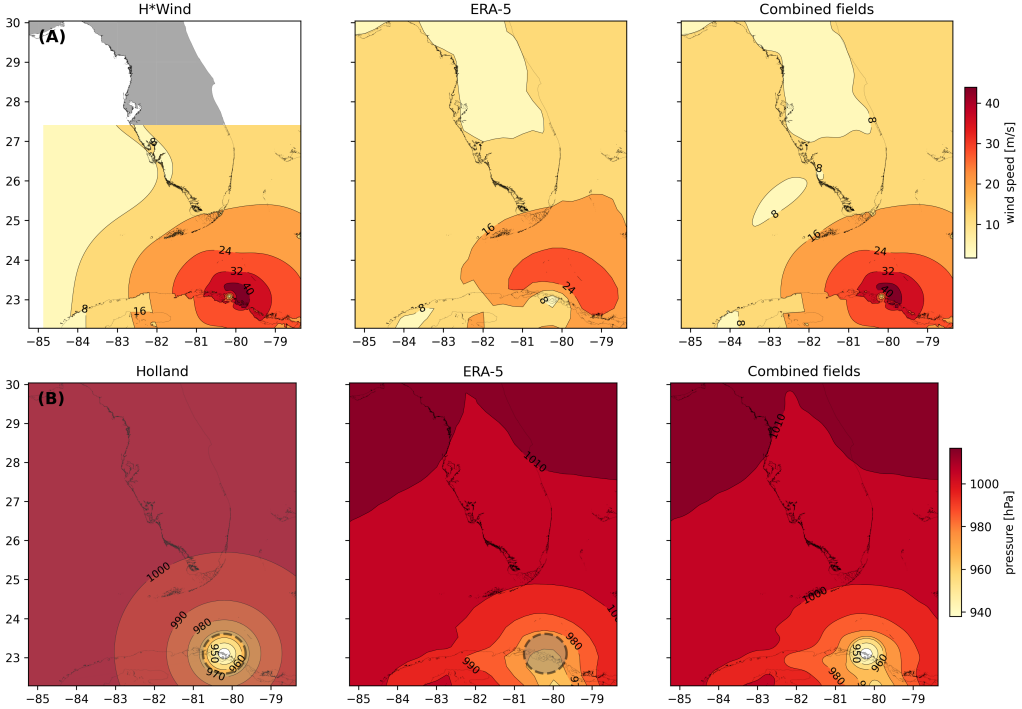


Fig. 2: Snapshot of the hybrid wind (**A**) and pressure (**B**) profiles constructed to capture the passage of Hurricane Irma at 1800 UTC on 9 September 2017. Wind profiles are obtained by combining high resolution H*Wind with coarser ERA-5 wind fields. The pressure field is built by combining the ERA-5 pressure field with an idealized Holland pressure profile based on the track of Irma in the HURDAT 2 database. Holland field was only used within the radius of maximum wind speed (dashed grey line) of the hurricane to capture its central depression.

of the hurricane based on its track as recorded in the HURDAT 2 database (Landsea and Franklin, 2013). Based on this information, the hybrid pressure field was constructed by combining an idealized Holland pressure profile (Lin and Chavas, 2012) within the radius of maximum wind speed of Irma (Knaff et al., 2018) with ERA-5 pressure field. The transition from the Holland profile to ERA-5 data outside the radius of maximum wind speed data was performed using a smooth step function (Fig. 2).

117 *2.3. Hydrodynamic model*

118 Ocean currents generated during hurricane Irma around South Florida
 119 were modelled using the 2D barotropic version of the unstructured-mesh
 120 coastal ocean model SLIM¹. The model mesh covers an area similar to the
 121 model extent of Dobbelaere et al. (2020b), that includes the FRT but also the
 122 Florida Straits and part of the Gulf of Mexico (Figure 1). However, this area
 123 has been slightly extended northeastward and westward in order to include
 124 the NOAA-NDBC buoys. Furthermore, to withstand potential cell drying
 125 during the hurricane, we solved the conservative shallow water equations with
 126 wetting-drying:

$$\begin{aligned} \frac{\partial H}{\partial t} + \nabla \cdot (\mathbf{U}) &= 0 , \\ \frac{\partial \mathbf{U}}{\partial t} + \nabla \cdot \left(\frac{\mathbf{U}\mathbf{U}}{H} \right) &= -f\mathbf{e}_z \times \mathbf{U} + \alpha g H \nabla(H - h) - \frac{1}{\rho} \nabla p_{\text{atm}} + \frac{1}{\rho} \boldsymbol{\tau}_s \quad (1) \\ &\quad + \nabla \cdot (\nu \nabla \mathbf{U}) - \frac{C_b}{H^2} |\mathbf{U}| \mathbf{U} + \gamma (\mathbf{U}_{\text{ref}} - \mathbf{U}) , \end{aligned}$$

127 where H is the water column height and \mathbf{U} is the depth-averaged transport;
 128 f is the Coriolis coefficient; g is the gravitational acceleration; h is the
 129 bathymetry; α is a coefficient stating whether the mesh element is wet ($\alpha = 1$)
 130 or dry ($\alpha = 0$) (Le et al., 2020); ν is the viscosity; C_b is the bulk bottom drag
 131 coefficient; p_{atm} is the atmospheric pressure; $\boldsymbol{\tau}_s$ is the surface stress, usually
 132 due to wind; and γ is a relaxation coefficient towards a reference transport \mathbf{U}_{ref} .
 133 As in Frys et al. (2020) and Dobbelaere et al. (2020b), SLIM currents were
 134 gradually relaxed towards the operational Navy HYCOM product (GOMl0.04²,
 135 Chassignet et al. (2007)) in regions where the water depth exceeds 50m.

136 At very high wind speeds, the white cap is blown off the crest of the
 137 waves. This phenomenon, also known as spumes, has been hypothesized to
 138 generate a layer of droplets that acts as a slip layer for the winds at the

¹<https://www.slim-ocean.be>

²<https://www.hycom.org/data/goml0pt04>

139 ocean-atmosphere interface (Holthuijsen et al., 2012). It causes a saturation
 140 of the wind drag coefficient for strong winds (Powell et al., 2003; Donelan
 141 et al., 2004; Curcic and Haus, 2020). We take this saturation effect into
 142 account by using the wind drag parameterization of Moon et al. (2007). In
 143 this parameterization, the drag coefficient C_d depends on the wind speed at
 144 10-m height U_{10} according to:

$$C_d = \kappa^2 \log \left(\frac{10}{z_0} \right)^{-2} \quad (2)$$

145 where κ is the von Karman constant and z_0 is the roughness length expressed
 146 as:

$$z_0 = \begin{cases} \frac{0.0185}{g} U_*^2 & \text{if } U_{10} \leq 12.5 \text{ m/s ,} \\ [0.085(-0.56U_*^2 + 20.255U_* + 2.458) - 0.58] \times 10^{-3} & \text{if } U_{10} > 12.5 \text{ m/s ,} \end{cases} \quad (3)$$

147 with U_* the friction velocity. The relation between U_{10} and U_* is given by:

$$U_{10} = -0.56U_*^2 + 20.255U_* + 2.458 . \quad (4)$$

148 The mesh resolution depends on the distance to the coastlines and reefs
 149 following the approach of Dobbelaere et al. (2020b). The mesh is then further
 150 refined according to bathymetry value and gradient, as suggested in the
 151 SWAN user-guide³. Such an approach improves the model efficiency as the
 152 mesh resolution is only increased where required by the currents and waves
 153 dynamics. The mesh was generated with the seamsh⁴ Python library, which is
 154 based on the open-source mesh generator GMSH (Geuzaine and Remacle,
 155 2009). It is composed of approximately 7.7×10^5 elements. The coarsest
 156 elements, far away from the FRT, has a characteristic length of about 5 km

³<http://swanmodel.sourceforge.net/unswan/unswan.htm>

⁴<https://pypi.org/project/seamsh/>

157 whereas the finest elements have a characteristic length of about 100 m along
158 the coastlines and over the reefs (Fig 1).

159 *2.4. Wave model*

160 Waves were modelled using the parallel unstructured-mesh version of the
161 Simulating WAves Nearshore (SWAN) model (Booij et al., 1999), one of the
162 most popular wave models for coastal areas and inland waters. It solves the
163 action balance equation (Mei, 1989):

$$\frac{\partial N}{\partial t} + \nabla_{\mathbf{x}} \cdot [(\mathbf{c}_g + \mathbf{u})N] + \frac{\partial}{\partial \theta}[c_\theta N] + \frac{\partial}{\partial \sigma}[c_\sigma N] = \frac{S_{in} + S_{ds} + S_{nl}}{\sigma}, \quad (5)$$

164 where $N = E/\sigma$ is the wave action density and E is the wave energy spectrum;
165 θ is the wave propagation direction; σ is the intrinsic wave frequency; \mathbf{c}_g is
166 the wave group velocity, $\mathbf{u} = \mathbf{U}/H$ is SLIM depth-averaged current velocity;
167 c_θ and c_σ are the propagation velocities in spectral space due to refraction
168 and shifting in frequency due to variations in depth and currents; and S_{in} ,
169 S_{ds} , and S_{nl} respectively represent wave growth by wind, wave decay and
170 nonlinear transfers of wave energy through interactions between triplets and
171 quadruplets. The wave spectra were discretized with 48 direction bins and 50
172 frequency bins logarithmically distributed from 0.03 to 2 Hz. Exponential
173 wind growth was parameterized using the formulation of Janssen (1991),
174 while dissipations by whitecapping and bottom dissipations followed the
175 formulations of Komen et al. (1984) and Madsen et al. (1989), respectively.
176 Coefficients for exponential wind growth and whitecapping parameterizations
177 were based on the results of Siadatmousavi et al. (2011), and significantly
178 differ from SWAN's default settings. By default, SWAN implements the
179 wind input formulation of Komen et al. (1984) and the steepness-dependent
180 coefficient governing dissipation by whitecapping is a linear function of the
181 wave number. In this study, this steepness-dependent coefficient is a quadratic
182 function of the wave number, as it showed better predictions of the significant
183 wave height in the study of Siadatmousavi et al. (2011). The choice of these

184 formulations was motivated by the appearance of numerical instabilities in
 185 the region of the Gulf Stream when using SWAN's default parameter values.
 186 Finally, wave boundary conditions were derived from WAVEWATCH III
 187 (Tolman et al., 2009) spectral outputs at NDBC buoy locations. We selected
 188 these datasets as the large number of NDBC buoys around our region of
 189 interest allowed for a fine representation of the wave spectra on the boundary
 190 of the domain.

191 Surface waves induce a net drift in the direction of the wave propagation,
 192 known as the Stokes drift (Van Den Bremer and Breivik, 2018; Stokes,
 193 1880). This net drift has a significant impact on sediment transport in
 194 nearshore regions (Hoefel and Elgar, 2003), on the formation of Langmuir
 195 cells (Langmuir, 1938; Craik and Leibovich, 1976) as well as on the transport
 196 of heat, salt or pollutants such as oil or micro-plastic in the upper ocean layer
 197 (McWilliams and Sullivan, 2000; Röhrs et al., 2012; Drivdal et al., 2014). To
 198 correctly model the Stokes drift profile in mixed wind-driven sea and swell
 199 conditions, the full two-dimensional wave spectrum must be represented by a
 200 spectral wave model within a wave-current coupling (Van Den Bremer and
 201 Breivik, 2018). We therefore used SWAN modelled spectra to compute the
 202 Stokes drift as follows:

$$\mathbf{u}_s = \int_0^{2\pi} \int_0^{+\infty} \frac{\sigma^3}{h \tanh(2kh)} E(\sigma, \theta) (\cos \theta, \sin \theta) d\sigma d\theta , \quad (6)$$

203 where k is the norm of the wave vector; h is the water depth; and $E(\sigma, \theta)$ is
 204 the wave energy density.

205 2.5. Coupled model

206 SLIM and SWAN are coupled so that they run on the same computational
 207 core and the same unstructured mesh. SLIM is run first and passes the
 208 wind velocity (\mathbf{U}_{10}), water level ($\eta = H - h$) and depth-averaged current
 209 ($\mathbf{u} = \mathbf{U}/H$) fields to SWAN, as well as a roughness length (z_0) for the bottom
 210 dissipation formulation of Madsen et al. (1989). This roughness length is

211 computed from SLIM’s bulk drag coefficient C_b following the approach of
212 Dietrich et al. (2011) so that both models have consistent bottom dissipation
213 parameterizations. SWAN then uses these quantities to compute the wave
214 radiation stress gradient, that is then passed to SLIM as the force exerted
215 by waves on currents τ_{wave} (Fig. 3). SLIM then uses this quantity to
216 update the value of the surface stress τ_s in Eq. (1), that now becomes
217 the sum of wind and wave-induced stresses $\tau_s = \tau_{\text{wind}} + \tau_{\text{wave}}$. Here, the
218 momentum flux from the atmosphere to the ocean is taken as the commonly-
219 used full wind stress τ_{wind} . Doing so, we neglect the momentum advected
220 away from the storm by the waves, leading to a 10-15% overestimation of the
221 momentum flux in hurricane winds (Curcic, 2015). Moreover, we followed
222 the approach of Dietrich et al. (2012) by characterizing the wave-induced
223 stresses using the radiation-stress representation instead of the vortex-force
224 representation (McWilliams et al., 2004). Although the later provides a clearer
225 and more meaningful decomposition of the wave effect, we implemented the
226 first representation for the sake of simplicity as it allows us to provide the
227 whole wave contribution as an additional surface stress to SLIM (Lane et al.,
228 2007).

229 SLIM’s governing equations are integrated using an implicit time inte-
230 gration scheme while SWAN is unconditionally stable (Dietrich et al., 2012),
231 allowing both models to be run with relatively large time steps. In this study,
232 the stationary version of SWAN was used, *i.e.* the time derivative of Eq. 5
233 was set to zero. This resulted in reduced scaling and convergence rates than
234 with the nonstationary version of SWAN but increased the stability of the
235 model. The wave spectra at each node of the mesh was saved at the end of
236 each iteration to serve as initial conditions for the next one. Both models
237 were run sequentially using a time step of 600 s, so that each computational
238 core was alternatively running either SLIM or SWAN. As in the coupling
239 between SWAN and ADCIRC (Dietrich et al., 2012), both models use the
240 same local sub-mesh, allowing for a one-to-one correspondence between the

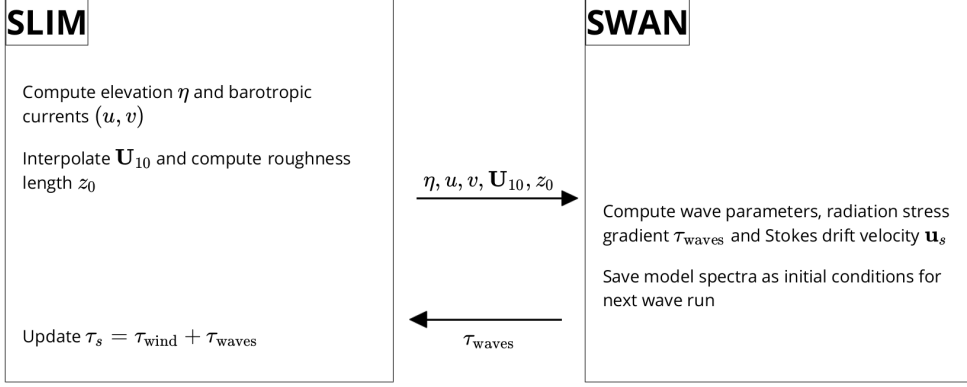


Fig. 3: Schematic illustration of the coupled SLIM+SWAN model.

241 geographic locations of the mesh vertices. No interpolation is therefore needed
 242 when passing the discretised variables from one model to the other, which
 243 allows an efficient inter-model communication. However, as SLIM is based on
 244 a discontinuous Galerkin finite element method, an additional conversion step
 245 to a continuous framework was required to transfer SLIM nodal quantities to
 246 SWAN.

247 *2.6. Quantifying the effect of wave-current interactions on transport*

248 To quantify the impact of wave-current interactions on transport processes,
 249 we compared the trajectories of passive particles advected by the uncoupled
 250 SLIM and coupled SLIM+SWAN currents during the passage of Irma in the
 251 Lower Keys. Furthermore, the depth-averaged Stokes drift was computed
 252 using the wave spectra of the coupled model SLIM+SWAN run as well as
 253 those of an uncoupled SWAN run. Particles were released on the inner and
 254 outer shelves at the points highlighted by red and blue dots in Fig. 4 on
 255 Sept. 7 at 0000 UTC and then tracked until Sept. 15. These initial particle
 256 positions were found using backtracking methods (Dobbelaeere et al., 2020a)
 257 to ensure that the release particles would intersect the path of Irma during
 258 its passage through the Florida Keys. We first defined two 25 km² circular
 259 regions on the trajectory of the hurricane (see red and blue circles in Fig. 4).

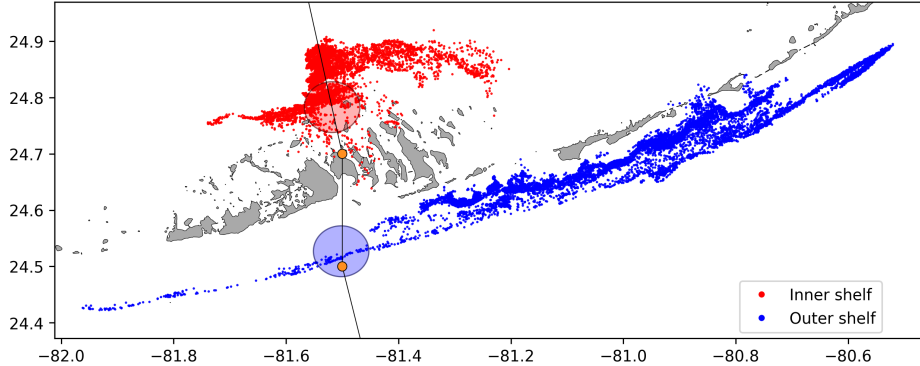


Fig. 4: Release regions of the passive particles on the inner and outer shelves (red and blue clouds) obtained by backtracking particles released in the red and blue circular areas during the passage of Irma.

260 Particles within these two regions were then tracked backward in time using
 261 uncoupled SLIM currents from the exact time of the passage of the hurricane
 262 until Sept. 7 at 0000 UTC. Their positions at the end of the backward
 263 simulation (see red and blue particle clouds in Fig. 4) corresponds to the
 264 initial condition of the forward transport simulations described below. We
 265 then compared the trajectories of particles originating from these regions and
 266 advected forward in time by different sets of currents: (i) uncoupled SLIM
 267 currents alone; (ii) coupled SLIM+SWAN currents; (iii) SLIM currents with
 268 the addition of the depth-averaged Stokes drift computed with the coupled
 269 wave-current model (Stokes-C); (iv) SLIM+SWAN currents with Stokes-C;
 270 and (v) SLIM currents with the depth-averaged Stokes drift computed with
 271 the uncoupled wave model (Stokes-U). Particles trajectories are compared by
 272 computing the distances between the centers of mass of the particle clouds
 273 through time.

274 **3. Results**

275 We first validated the reconstructed atmospheric fields of hurricane Irma
 276 as well as the outputs of our coupled wave-current model against field mea-

surements. A summary of the error statistics is given in Table 1. We then used the validated model outputs to simulate the transport of passive drifters in the Lower Keys during the passage of Hurricane Irma. These drifters were advected by the sets of currents described in section 2.6 and their trajectories were compared to evaluate the impact of the wave-current interactions and the Stokes drift on the transport processes during the passage of Irma.

3.1. Model validation

H^* Wind winds and hybrid pressure field agree well with station measurements at Vaca Key station (Fig. 5). The hybrid pressure field shows a better agreement with observations than ERA-5 pressure as it successfully reproduces the storm depression. ERA-5 fields, on the other hand, fail to reproduce the low pressure at the core of the hurricane due to their coarser grid, leading to an overestimation of 8 mbar of the storm depression. Both H^* Wind and ERA-5 agree well with observed wind speeds although both data sets tend to slightly overestimate the width and intensity of the wind peak. However, H^* wind profiles better reproduce the timing of the observed peak, as ERA-5 winds tend to anticipate it. H^* wind also exhibits a slightly narrower peak in wind speed, which better agrees with observations.

Hydrodynamic outputs of the coupled wave-current model agree well with tide gauge (Fig. 6) and ADCP measurements (Fig. 7). Despite a slight overestimation of the amplitude of sea surface elevation (Table 1) in fair weather conditions, the timing and amplitude of the storm surges are well reproduced by the coupled model. The largest model error during the surge is an overestimation of 18 cm of the elevation peak at Virginia Key. The fit is especially good at Naples, where both the large positive and negative surges are captured by the coupled model with an error of less than 5 cm. Modelled 2D currents were validated against depth-averaged ADCP measurements at mooring stations C10, C12 and C13 (Fig. 7). As in Liu et al. (2020), we performed the vector correlation analysis of Kundu (1976) to compare modelled and observed current velocity vectors. Correlation coefficients (ρ)

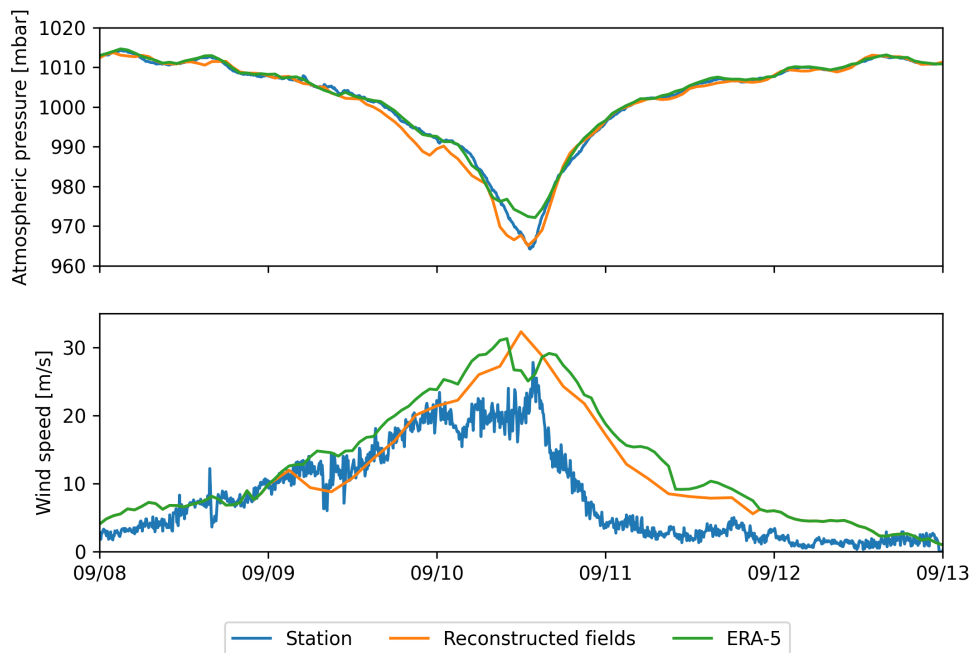


Fig. 5: Comparison of reconstructed wind atmospheric pressure with field measurements and coarser ECMWF ERA-5 profiles at Vaca Key station. The generated hybrid atmospheric forcings better reproduce the observed storm depression while H*wind winds better reproduce the measured peak in wind speed.

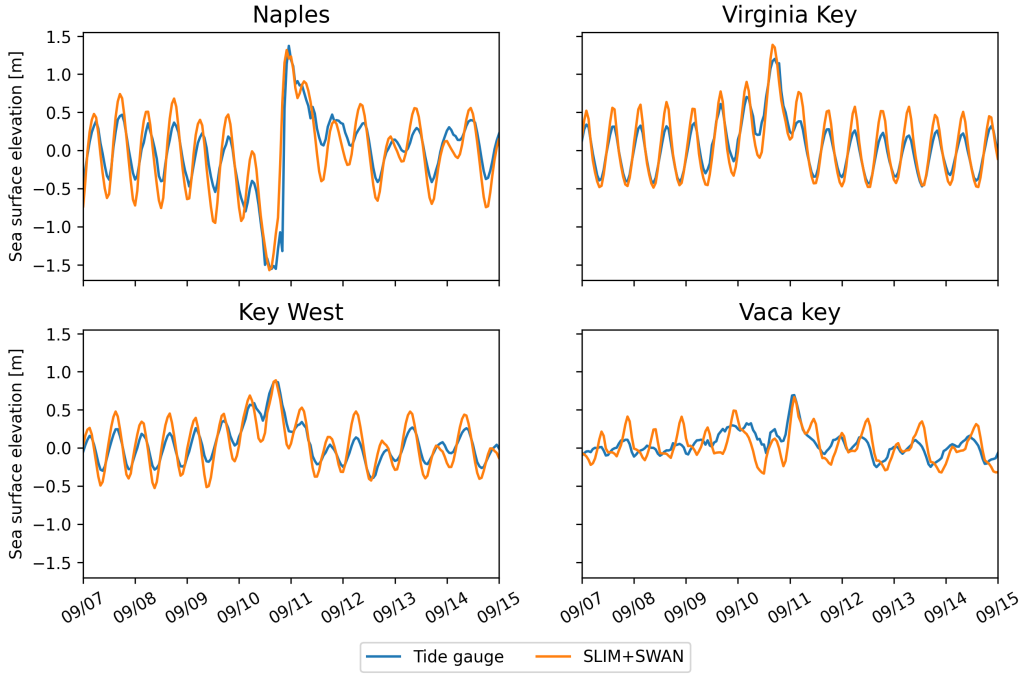


Fig. 6: Comparison of modelled sea surface elevation at the 4 tide gauges shown in Fig. 1B. The timing and amplitudes of the storm surges are well reproduced by the model

307 between simulated and observed depth-averaged currents are 0.84, 0.74 and
 308 0.73 at stations C10, C12 and C13, respectively. Average veering angles were
 309 computed as well and are below 12° , as in (Liu et al., 2020). Furthermore, our
 310 model tends to produce larger prediction errors on the northward component
 311 of the depth-averaged currents than the eastward one (Table 1). [replace
 312 by summary of information of Table] As expected from a depth-averaged
 313 model, the best fit with observations is obtained at the shallowest mooring
 314 C10, located on the 25 m isobath, with an average veering angle of 6° and
 315 smaller error statistics (Table 1).

316 The simulated significant wave height agrees well with observations on
 317 the WFS, where errors on the peak value do not exceed 5% (Fig. 8). On
 318 Florida's eastern shelf, errors are slightly larger and reach 20%. Although the
 319 model outputs agree well with observations, a lag in significant wave height is

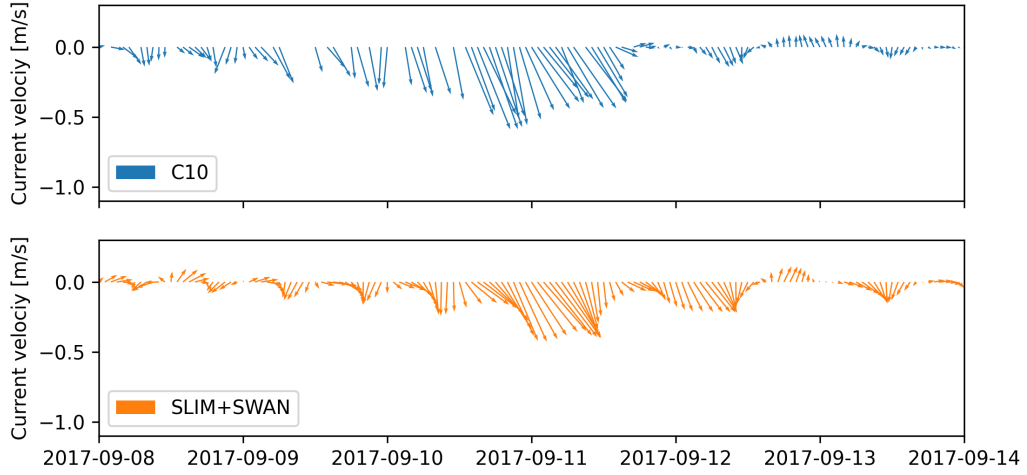


Fig. 7: Comparison of modelled current velocity with observed velocity at mooring C10 (see Fig. 1B for its location). Modelled current velocities agree well with observations, with a correlation coefficient of 0.83 and an average veering angle of 6° .

observed for all 4 buoys. Moreover, the peak in significant wave height tends to be underestimated at buoys 41113 and 41114, located on the East Florida Shelf. Other wave parameters were better reproduced by the model on the WFS as well (see buoy 42036 in Fig. 8 and Table 1).

3.2. Impact of waves on currents and transport

We evaluated the impact of wave-current interactions on modelled currents during the passage of Irma in the Lower Keys, between Sept. 7 and 13, 2017. First, we computed the maximum difference between currents modelled by SLIM and SLIM+SWAN during this period (Fig. 9A). The largest differences in current speed were observed over the reefs [insist on large wave dissipation on offshore reefs → protection barrier], on the shelf break and around islands. They can locally reach 1 m/s, with the coupled SLIM+SWAN model yielding the largest amplitudes. The regions where the differences are the largest experience the largest wave-induced stress τ_{wave} (Fig. 9B), as wave breaking and wave slowing down over rough seabed induce variations of the wave radiation stress (Longuet-Higgins and Stewart, 1964). Wave-induced differences in

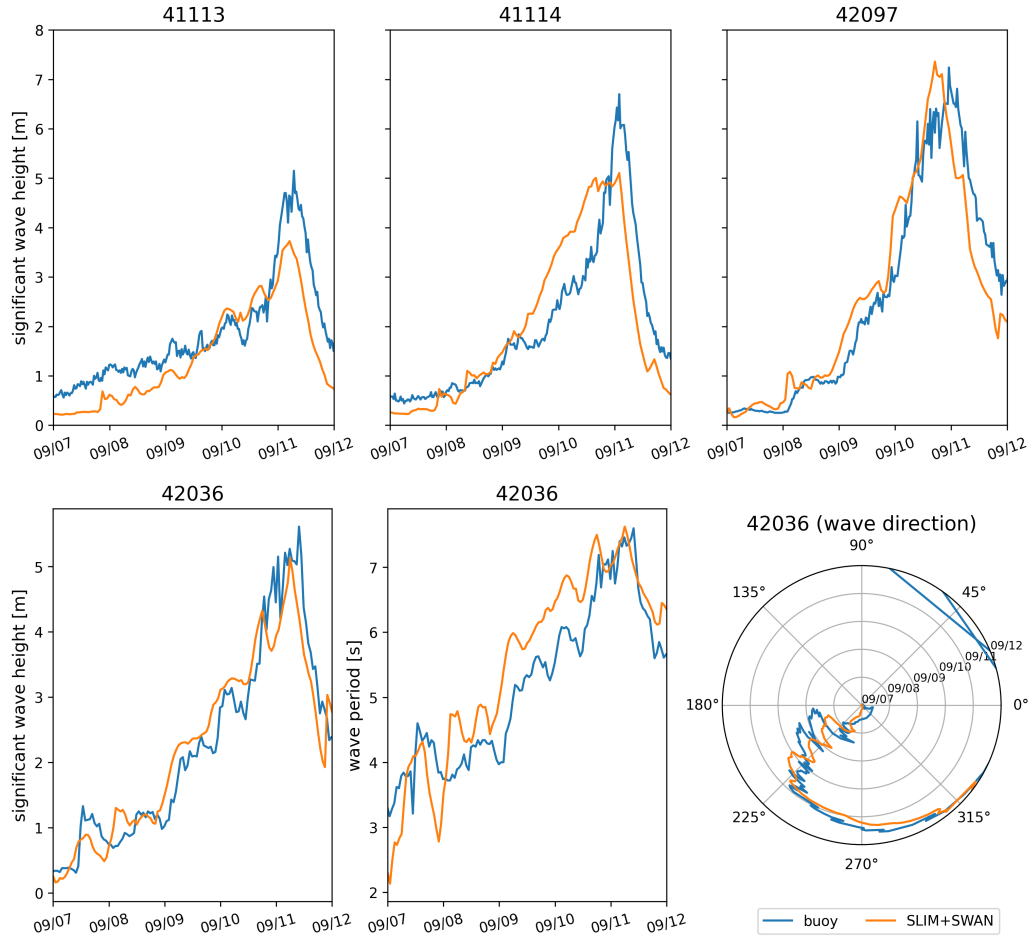


Fig. 8: Comparison of modelled wave parameters with observation at the 4 buoys location (locations shown in Fig. 1B). Modelled significant wave height agrees well with field measurement.

Station	Variable	Bias	MAE	RMSE
Vaca Key	sse (m)	n/a	0.12	0.16
	U_{10} (m/s)	1.51	1.85	2.61
	p_{atm} (hPa)	-0.21	0.59	1.03
Key West	sse (m)	n/a	0.11	0.13
Virginia Key	sse (m)	n/a	0.10	0.13
Naples	sse (m)	n/a	0.18	0.23
C10	u (m/s)	-0.006	0.04	0.05
	v (m/s)	0.02	0.06	0.08
C12	u (m/s)	-0.01	0.06	0.07
	v (m/s)	0.06	0.09	0.11
C13	u (m/s)	0.004	0.06	0.08
	v (m/s)	0.04	0.06	0.08
41113	H_s (m)	-0.35	0.40	0.51
	T_m (s)	-2.18	2.47	3.13
41114	H_s (m)	-0.21	0.53	0.68
	T_m (s)	-1.69	2.53	3.15
42036	H_s (m)	-0.03	0.26	0.36
	T_m (s)	0.04	0.65	0.77
42097	H_s (m)	-0.15	0.40	0.57
	T_m (s)	0.02	0.62	0.74

Table 1: Error statistics comparing SLIM+SWAN simulated quantities with the measured sea surface elevation (sse), eastward and northward depth-average current velocities (u,v), significant wave height (H_s), and zero-crossing mean wave period (T_m). Model bias, mean absolute error (MAE), and root mean squared error (RMSE) are listed by variable (unit) and value.

336 current speed were amplified by the action of the wind stress τ_{wind} (Fig. 9C).
337 Wind speeds were larger in the front right quadrant of the hurricane (Zedler
338 et al., 2009), yielding larger differences on the right-hand side of the storm
339 trajectory. This is especially clear in the area between the Florida Keys and
340 the Everglades, where relatively small values of τ_{wave} nonetheless produce
341 current speed differences of up to 0.5 m/s because of the wind stress.

342 Waves play a significant role on the transport processes during and after
343 the passage of hurricane Irma (Fig. 10A). Comparing SLIM and SLIM+SWAN
344 shows that wave-current interactions alone yield differences of up to 5 km
345 between the modelled trajectories on the passage of the hurricane. These
346 differences exceed 10 km on the outer shelf when Stokes drift is taken into
347 account. The impact of the waves on the transport processes differs signifi-
348 cantly between the inner and outer shelves, with wave-induced differences in
349 trajectories 4 to 5 times larger on the outer shelf. Furthermore, the distances
350 between the centers of mass of the clouds of particles tend to stabilize on
351 the inner shelf after the passage of Irma, while they keep increasing on the
352 other shelf up to two days after the passage of the hurricane when taking
353 Stokes drift into account. These distances then stabilize for about a day
354 before they start decreasing (see right panel of Fig. 10A). However, when
355 considering wave-current interactions alone (SLIM vs. SLIM+SWAN), the
356 distance between the clouds of particles starts to decrease just after the
357 passage of Irma.

358 The Stokes drift appears to have a larger effect than the radiation stress
359 gradient and the wave-current interactions (Fig 10A). Nonetheless, comparing
360 the different curves for the outer shelf suggests that the radiation-stress
361 gradient induces effects similar to the impact of the Stokes drift in this region
362 during the passage of Irma. However, comparing SLIM and SLIM+SWAN
363 both on the inner and other shelf, we see that this impact is negligible during
364 the rest of the simulation. Moreover, comparison of Stokes-U and Stokes-C
365 (Fig. 10B) indicates that the difference between the trajectories of particles

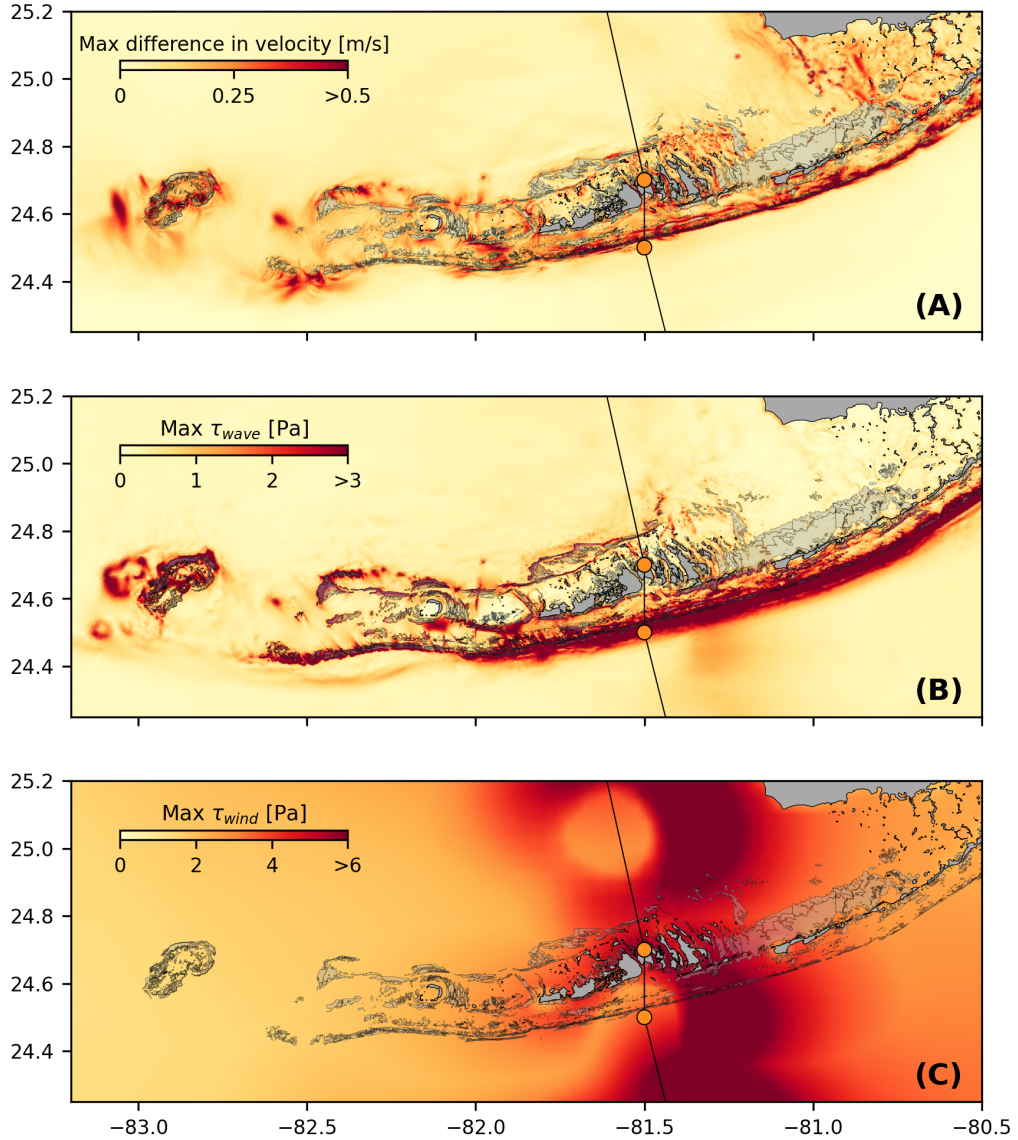


Fig. 9: (A). Maximum difference between SLIM and SLIM+SWAN currents during the passage of Irma in the Lower Florida Keys; (B) Maximum wave radiation stress gradient τ_{wave} and (C) maximum wind stress τ_{wind} (C) generated by the hurricane. Wave-induced stress yields difference larger than 0.5 m/s in current velocities.

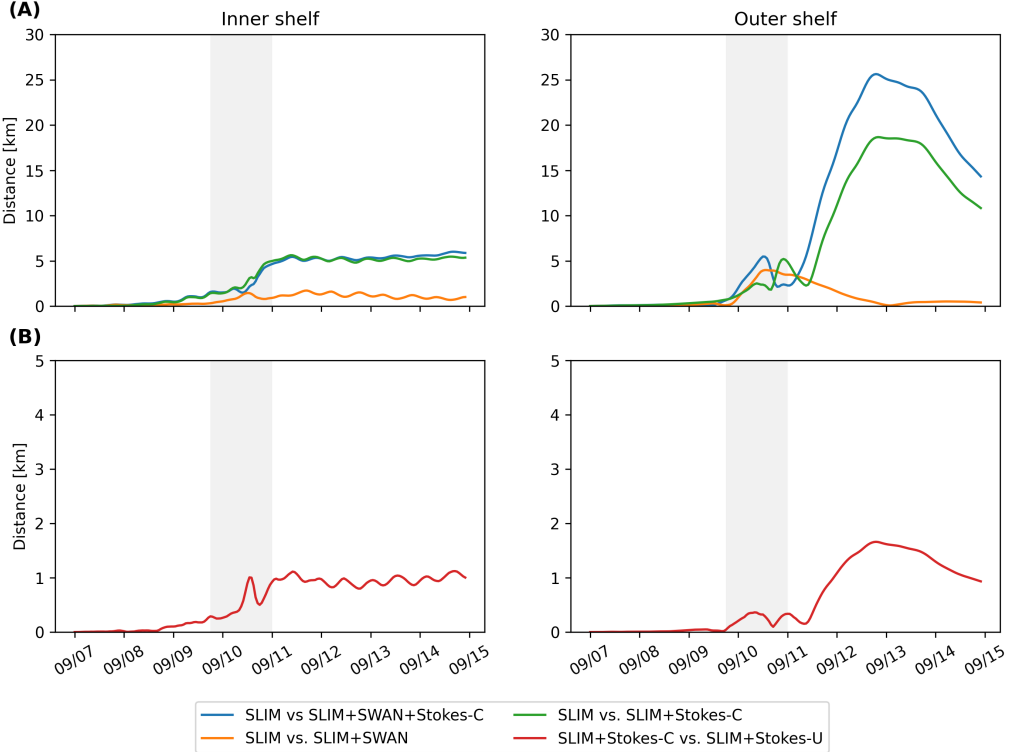


Fig. 10: Difference between the centers of mass of the particle clouds released from the regions highlighted in Fig. 4 and advected by different combinations of coupled and uncoupled velocity fields. Matthieu: prsenter plus d'informations sur la Figure 8, notamment les nuages de points issus des deux simulations (SLIM et SLIM+SWAN+Stokes-C), ainsi que les centres de masses correspondants. Ca devrait permettre de soutenir la partie rsultats.

adverted by the two Stokes drift do not exceed 2 km, with larger discrepancies on the outer shelf. The sudden increase of 'SLIM+Stokes-C vs SLIM+Stokes-U' curves on the passage of Irma (and two days after on the outer shelf) and their stabilization afterwards suggest that taking wave-currents interactions into account when modeling waves mostly has an impact during (and directly after) the passage of the hurricane.

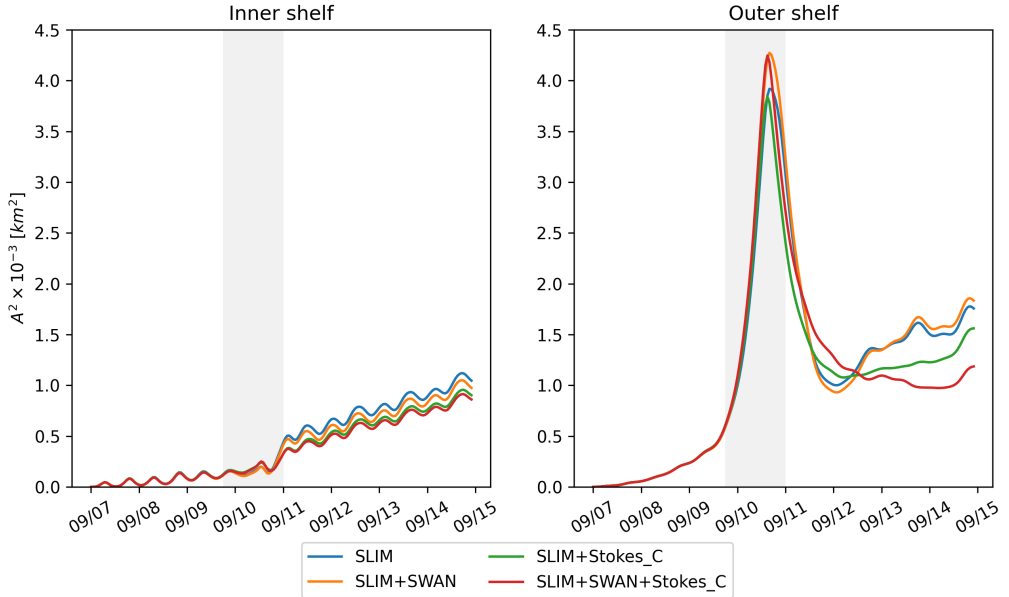


Fig. 11: Dispersion of particles with different velocity fields → not sure to know what to say about that...

372 4. Discussion

373 Our results show that neglecting wave effects can induce differences of up
 374 to 1 m/s in modelled current velocities, leading to variations of more than 10
 375 km in modelled trajectories. These differences in modelled trajectories were
 376 significantly larger and required more time to stabilize on the outer shelf. The
 377 impact of the Stokes drift dominates the effects of wave-current interactions
 378 through the radiation stress gradient, except at the moment of the passage
 379 of the hurricane, when both contributions are similar. Finally, neglecting
 380 wave-current interactions when computing Stokes drift lead to variations of
 381 up to 2 km in modelled trajectories on the passage of the hurricane.

382 Despite slightly overestimating the amplitude of the sea surface elevation
 383 in fair weather conditions, the coupled model reproduces correctly the timing
 384 and amplitude of the observed storm surge (Fig. 6). All elevation peaks are
 385 captured with a 4% accuracy at every stations except Virginia key, where the

386 surge was overestimated by about 15%. Such accuracy is key to predict the
387 damages caused by the hurricane, as most destroyed and severely damaged
388 buildings in the Florida keys during Hurricane Irma were caused by storm
389 surge and waves (Xian et al., 2018). Furthermore, the high resolution of
390 model in the regions captures flow accelerations between islands and reefs,
391 allowing for a precise representation of the surge risk in the Florida Keys. In
392 addition to accurately capture positive surges, the model also reproduced the
393 observed negative surge in Naples with an error of about 1%. This result is
394 of interest from a biological point of view as negative surges, although less
395 studied, affect water exchanges between the estuaries and the coastal ocean
396 and disturb the benthic ecosystems (Liu et al., 2020). Such rapid decrease
397 in water level followed by a positive surge cause massive freshwater inflows,
398 generating a significant decrease in water salinity (Wachnicka et al., 2019).

399 Strong currents such as the Gulf Stream affect waves through refraction
400 over gradients in current velocity, shoaling and breaking of opposing waves
401 or lengthening of following waves (Hegermiller et al., 2019). Under hurri-
402 cane conditions, these interactions can cause numerical instabilities in the
403 wave model if appropriate parameterizations and model resolution are not
404 applied. Hegermiller et al. (2019), for instance, used a 5-km model grid and
405 48 directional bins to capture spatial gradients in wave height induced by
406 wave-currents interactions in the Gulf Stream during Hurricane Matthew
407 (2016). These guidelines were followed when defining the coarsest resolution of
408 the model mesh as well as the spectral discretization of SWAN. Boundary con-
409 ditions and directional spreading of the incident waves also play a significant
410 role when modeling wave-current interactions at meso- and submesoscales
411 (Villas Bôas et al., 2020), which motivated our choice of imposing full spectra
412 on the boundary of the wave model instead of bulk parameters. Finally,
413 SWAN default parameterizations for wind energy input and whitecapping
414 caused numerical instabilities by overestimating wave growth and steepness
415 on the boundary of the Gulf Stream on the passage of Irma. This overes-

416 timation was solved by using the parameterization of Siadatmousavi et al.
417 (2011). The parameters used in this study were calibrated on the Northern
418 Gulf of Mexico, which might explains that our model better reproduces wave
419 parameters at buoys 42036 and 4207, located on the WFS. However, these
420 calibrated parameters might underestimate wind-induced wave growth might
421 underestimate Florida's eastern shelf. Consequently, incident wave do not
422 receive enough energy to grow after breaking on the bank boundary, leading
423 to the underestimation of the significant wave height at buoys 41113 and
424 41114. A more extensive calibration study might therefore be necessary to
425 achieve good agreement with field measurements on both sides of Florida.
426 Nonetheless, as this study focuses on the wave produced by Irma, which
427 made landfall on the western coasts of Florida, the use of parameterizations
428 calibrated for the Gulf of Mexico seems reasonable.

429 Wave impact during Irma is different on the inner and outer shelves. It is
430 less important on the inner shelf because of the sheltering of the inner shelf
431 due to reefs and islands as well as wave breaking on the shelf break. The inner
432 shelf hence experiences weaker waves and currents, inducing weaker and more
433 localized transport. Furthermore, the impact of winds on waves is reduced
434 in shallower areas under the action of depth-induced breaking. This might
435 explain why differences between particle trajectories stabilize on the inner
436 shelf just after the passage of Hurricane Irma. However, the Florida Keys
437 still experienced strong winds after the passage of the core of the hurricane,
438 which generated high waves in the deeper areas. This might explain why the
439 differences on between the modelled trajectories kept increasing on the outer
440 shelf under the action of strong Stokes drift up to two days after the passage
441 of the hurricane.

442 [Rephrase to avoid 'X vs Y'] Differences between the trajectories of particles
443 advected by SLIM+Stokes-C or SLIM+Stokes-U, do not exceed 2 km (Fig.
444 10). This suggest that taking wave-currents interactions into account when
445 computing Stokes drift, even under hurricane conditions yields a limited

446 impact. Furthermore, the curves 'SLIM vs. SLIM+SWAN+Stokes-C' and
447 'SLIM vs. SLIM+Stokes-C' show similar values, which seems to indicate that
448 wave impact of currents is limited on the inner shelf. This would suggest that it
449 is not necessary to take wave-current interactions into account when modeling
450 the trajectories of tracers in shallow, sheltered areas such as the inner WFS
451 during a hurricane. Uncoupled currents with uncoupled Stokes drift should
452 give a reasonably accurate approximation of the transport processes. However,
453 this does not hold for deeper regions, as highlighted by the differences between
454 'SLIM vs. SLIM+SWAN+Stokes-C' and 'SLIM+Stokes-C' in the outer shelf.

- 455 • Broad perspective \Rightarrow not limited to FL, mention search and rescue

456 5. Conclusion

457 We developed a coupled wave-current model to study the impact of
458 waves on transport processes during Hurricane Irma. In order to accurately
459 represent the wind and pressure profiles of the hurricane, we built hybrid fields
460 by combining coarser ERA-5 data with high-resolution H*Wind data for
461 the wind speed and idealized Holland profiles for the pressure. Comparing
462 these hybrid profiles with field observations showed that they were better at
463 reproducing the observed central depression of the hurricane as well as the
464 peak in wind speed than ERA-5 data. Using these hybrid fields as forcings,
465 our coupled model accurately reproduced the storm surge at NDBC buoy
466 locations and produced currents and wave parameters in good agreement
467 with field observations, especially on the WFS. The modelled currents and
468 Stokes drift were then used to evaluate the impact of waves on the trajectory
469 of passive drifters on the passage of the hurricane through the Florida Keys.

470 Acknowledgments

471 Computational resources were provided by the Consortium des Équipements
472 de Calcul Intensif (CÉCI), funded by the F.R.S.-FNRS under Grant No.

⁴⁷³ 2.5020.11. Thomas Dobbelaere is a PhD student supported by the Fund for
⁴⁷⁴ Research training in Industry and Agriculture (FRIA/FNRS).

⁴⁷⁵ **References**

- ⁴⁷⁶ Bever, A.J., MacWilliams, M.L., 2013. Simulating sediment transport pro-
⁴⁷⁷ cesses in San Pablo Bay using coupled hydrodynamic, wave, and sediment
⁴⁷⁸ transport models. *Marine Geology* 345, 235–253.
- ⁴⁷⁹ Bhatia, K.T., Vecchi, G.A., Knutson, T.R., Murakami, H., Kossin, J., Dixon,
⁴⁸⁰ K.W., Whitlock, C.E., 2019. Recent increases in tropical cyclone intensifi-
⁴⁸¹ cation rates. *Nature Communications* 10, 1–9.
- ⁴⁸² Booij, N., Ris, R.C., Holthuijsen, L.H., 1999. A third-generation wave
⁴⁸³ model for coastal regions: 1. Model description and validation. *Journal of*
⁴⁸⁴ *Geophysical Research: Oceans* 104, 7649–7666.
- ⁴⁸⁵ Breivik, Ø., Allen, A.A., Maisondieu, C., Olagnon, M., 2013. Advances in
⁴⁸⁶ search and rescue at sea. *Ocean Dynamics* 63, 83–88.
- ⁴⁸⁷ Chassignet, E.P., Hurlburt, H.E., Smedstad, O.M., Halliwell, G.R., Hogan,
⁴⁸⁸ P.J., Wallcraft, A.J., Baraille, R., Bleck, R., 2007. The HYCOM (hybrid
⁴⁸⁹ coordinate ocean model) data assimilative system. *Journal of Marine*
⁴⁹⁰ *Systems* 65, 60–83.
- ⁴⁹¹ Chen, C., Huang, H., Beardsley, R.C., Liu, H., Xu, Q., Cowles, G., 2007.
⁴⁹² A finite volume numerical approach for coastal ocean circulation studies:
⁴⁹³ Comparisons with finite difference models. *Journal of Geophysical Research:*
⁴⁹⁴ *Oceans* 112.
- ⁴⁹⁵ Craik, A.D., Leibovich, S., 1976. A rational model for Langmuir circulations.
⁴⁹⁶ *Journal of Fluid Mechanics* 73, 401–426.
- ⁴⁹⁷ Curcic, M., 2015. Explicit air-sea momentum exchange in coupled atmosphere-
⁴⁹⁸ wave-ocean modeling of tropical cyclones. Ph.D. thesis.

- 499 Curcic, M., Chen, S.S., Özgökmen, T.M., 2016. Hurricane-induced ocean
500 waves and stokes drift and their impacts on surface transport and dispersion
501 in the Gulf of Mexico. *Geophysical Research Letters* 43, 2773–2781.
- 502 Curcic, M., Haus, B.K., 2020. Revised estimates of ocean surface drag in
503 strong winds. *Geophysical Research Letters* 47, e2020GL087647.
- 504 Dietrich, J., Bunya, S., Westerink, J., Ebersole, B., Smith, J., Atkinson,
505 J., Jensen, R., Resio, D., Luettich, R., Dawson, C., et al., 2010. A high-
506 resolution coupled riverine flow, tide, wind, wind wave, and storm surge
507 model for southern Louisiana and Mississippi. Part II: Synoptic description
508 and analysis of Hurricanes Katrina and Rita. *Monthly Weather Review*
509 138, 378–404.
- 510 Dietrich, J., Westerink, J., Kennedy, A., Smith, J., Jensen, R., Zijlema, M.,
511 Holthuijsen, L., Dawson, C., Luettich, R., Powell, M., et al., 2011. Hurricane
512 Gustav (2008) waves and storm surge: Hindcast, synoptic analysis, and
513 validation in southern Louisiana. *Monthly Weather Review* 139, 2488–2522.
- 514 Dietrich, J.C., Tanaka, S., Westerink, J.J., Dawson, C., Luettich, R., Zijlema,
515 M., Holthuijsen, L.H., Smith, J., Westerink, L., Westerink, H., 2012. Per-
516 formance of the unstructured-mesh, SWAN+ ADCIRC model in computing
517 hurricane waves and surge. *Journal of Scientific Computing* 52, 468–497.
- 518 Dobbelaere, T., Muller, E., Gramer, L., Holstein, D., Hanert, E., 2020a.
519 Report on the potential origin of the SCTLD in the Florida Reef Tract.
520 Available online at: [https://floridadep.gov/rcp/coral/documents/
521 report-potential-origin-sctld-florida-reef-tract](https://floridadep.gov/rcp/coral/documents/report-potential-origin-sctld-florida-reef-tract).
- 522 Dobbelaere, T., Muller, E.M., Gramer, L.J., Holstein, D.M., Hanert, E., 2020b.
523 Coupled epidemic-hydrodynamic modeling to understand the spread of a
524 deadly coral disease in Florida. *Frontiers in Marine Science* 7, 1016.

- 525 Donelan, M., Haus, B., Reul, N., Plant, W., Stiassnie, M., Gruber, H., Brown,
526 O., Saltzman, E., 2004. On the limiting aerodynamic roughness of the
527 ocean in very strong winds. *Geophysical Research Letters* 31.
- 528 Drivdal, M., Broström, G., Christensen, K., 2014. Wave-induced mixing and
529 transport of buoyant particles: Application to the Statfjord A oil spill.
530 *Ocean Science* 10, 977–991.
- 531 Figueiredo, J., Baird, A.H., Connolly, S.R., 2013. Synthesizing larval com-
532 petence dynamics and reef-scale retention reveals a high potential for
533 self-recruitment in corals. *Ecology* 94, 650–659.
- 534 Frys, C., Saint-Amand, A., Le Hénaff, M., Figueiredo, J., Kuba, A., Walker,
535 B., Lambrechts, J., Vallaeyns, V., Vincent, D., Hanert, E., 2020. Fine-scale
536 coral connectivity pathways in the Florida Reef Tract: Implications for
537 conservation and restoration. *Frontiers in Marine Science* 7, 312.
- 538 Geuzaine, C., Remacle, J.F., 2009. Gmsh: A 3-d finite element mesh generator
539 with built-in pre-and post-processing facilities. *International journal for
540 numerical methods in engineering* 79, 1309–1331.
- 541 Harper, B., Kepert, J., Ginger, J., 2010. Guidelines for converting between
542 various wind averaging periods in tropical cyclone conditions.
- 543 Hegermiller, C.A., Warner, J.C., Olabarrieta, M., Sherwood, C.R., 2019.
544 Wave-current interaction between Hurricane Matthew wave fields and the
545 Gulf Stream. *Journal of Physical Oceanography* 49, 2883–2900.
- 546 Hoefel, F., Elgar, S., 2003. Wave-induced sediment transport and sandbar
547 migration. *Science* 299, 1885–1887.
- 548 Holthuijsen, L.H., Powell, M.D., Pietrzak, J.D., 2012. Wind and waves in
549 extreme hurricanes. *Journal of Geophysical Research: Oceans* 117.

- 550 Janssen, P.A., 1991. Quasi-linear theory of wind-wave generation applied to
551 wave forecasting. *Journal of Physical Oceanography* 21, 1631–1642.
- 552 Johns, W.E., Schott, F., 1987. Meandering and transport variations of the
553 Florida Current. *Journal of Physical Oceanography* 17, 1128–1147.
- 554 Knaff, J.A., Sampson, C.R., Musgrave, K.D., 2018. Statistical tropical cyclone
555 wind radii prediction using climatology and persistence: Updates for the
556 western North Pacific. *Weather and Forecasting* 33, 1093–1098.
- 557 Komen, G., Hasselmann, S., Hasselmann, K., 1984. On the existence of a
558 fully developed wind-sea spectrum. *Journal of Physical Oceanography* 14,
559 1271–1285.
- 560 Kossin, J.P., Knapp, K.R., Olander, T.L., Velden, C.S., 2020. Global increase
561 in major tropical cyclone exceedance probability over the past four decades.
562 *Proceedings of the National Academy of Sciences* 117, 11975–11980.
- 563 Kourafalou, V.H., Kang, H., 2012. Florida Current meandering and evo-
564 lution of cyclonic eddies along the Florida Keys Reef Tract: Are they
565 interconnected? *Journal of Geophysical Research: Oceans* 117.
- 566 Kundu, P.K., 1976. Ekman veering observed near the ocean bottom. *Journal*
567 *of Physical Oceanography* 6, 238–242.
- 568 Landsea, C.W., Franklin, J.L., 2013. Atlantic hurricane database uncertainty
569 and presentation of a new database format. *Monthly Weather Review* 141,
570 3576–3592.
- 571 Lane, E.M., Restrepo, J., McWilliams, J.C., 2007. Wave-current interaction:
572 A comparison of radiation-stress and vortex-force representations. *Journal*
573 *of physical oceanography* 37, 1122–1141.
- 574 Langmuir, I., 1938. Surface motion of water induced by wind. *Science* 87,
575 119–123.

- 576 Le, H.A., Lambrechts, J., Ortleb, S., Gratiot, N., Deleersnijder, E., Soares-
577 Frazão, S., 2020. An implicit wetting–drying algorithm for the discontinuous
578 galerkin method: application to the tonle sap, mekong river basin. Environmental
579 Fluid Mechanics , 1–29.
- 580 Le Hénaff, M., Kourafalou, V.H., Paris, C.B., Helgers, J., Aman, Z.M., Hogan,
581 P.J., Srinivasan, A., 2012. Surface evolution of the Deepwater Horizon
582 oil spill patch: Combined effects of circulation and wind-induced drift.
583 Environmental Science & Technology 46, 7267–7273.
- 584 Lee, T.N., Leaman, K., Williams, E., Berger, T., Atkinson, L., 1995. Florida
585 Current meanders and gyre formation in the southern Straits of Florida.
586 Journal of Geophysical Research: Oceans 100, 8607–8620.
- 587 Lee, T.N., Mayer, D.A., 1977. Low-frequency current variability and spin-off
588 eddies along the shelf off southeast Florida. Collected Reprints 1, 344.
- 589 Lee, T.N., Smith, N., 2002. Volume transport variability through the Florida
590 Keys tidal channels. Continental Shelf Research 22, 1361–1377.
- 591 Lee, T.N., Williams, E., 1988. Wind-forced transport fluctuations of the
592 Florida Current. Journal of Physical Oceanography 18, 937–946.
- 593 Li, Z., Johns, B., 1998. A three-dimensional numerical model of surface
594 waves in the surf zone and longshore current generation over a plane beach.
595 Estuarine, Coastal and Shelf Science 47, 395–413.
- 596 Lin, N., Chavas, D., 2012. On hurricane parametric wind and applications in
597 storm surge modeling. Journal of Geophysical Research: Atmospheres 117.
- 598 Liu, Y., Weisberg, R.H., 2012. Seasonal variability on the West Florida shelf.
599 Progress in Oceanography 104, 80–98.

- 600 Liu, Y., Weisberg, R.H., Zheng, L., 2020. Impacts of hurricane Irma on the
601 circulation and transport in Florida Bay and the Charlotte Harbor estuary.
602 *Estuaries and Coasts* 43, 1194–1216.
- 603 Liubartseva, S., Coppini, G., Lecci, R., Clementi, E., 2018. Tracking plastics
604 in the Mediterranean: 2D Lagrangian model. *Marine Pollution Bulletin*
605 129, 151–162.
- 606 Longuet-Higgins, M.S., 1970. Longshore currents generated by obliquely
607 incident sea waves. *Journal of geophysical research* 75, 6778–6789.
- 608 Longuet-Higgins, M.S., Stewart, R., 1964. Radiation stresses in water waves;
609 a physical discussion, with applications, in: Deep sea research and oceano-
610 graphic abstracts, Elsevier. pp. 529–562.
- 611 Madsen, O.S., Poon, Y.K., Gruber, H.C., 1989. Spectral wave attenuation by
612 bottom friction: Theory, in: *Coastal Engineering 1988*, pp. 492–504.
- 613 McWilliams, J.C., Restrepo, J.M., Lane, E.M., 2004. An asymptotic theory
614 for the interaction of waves and currents in coastal waters. *Journal of Fluid*
615 *Mechanics* 511, 135.
- 616 McWilliams, J.C., Sullivan, P.P., 2000. Vertical mixing by Langmuir circula-
617 tions. *Spill Science & Technology Bulletin* 6, 225–237.
- 618 Mei, C.C., 1989. The applied dynamics of ocean surface waves. volume 1.
619 World scientific.
- 620 Moon, I.J., Ginis, I., Hara, T., Thomas, B., 2007. A physics-based parame-
621 terization of air-sea momentum flux at high wind speeds and its impact on
622 hurricane intensity predictions. *Monthly Weather Review* 135, 2869–2878.
- 623 Pinelli, J.P., Roueche, D., Kijewski-Correa, T., Plaz, F., Prevatt, D., Zisis,
624 Elawady, A., Haan, F., Pei, S., Gurley, K., et al., 2018. Overview of
625 damage observed in regional construction during the passage of Hurricane

- 626 Irma over the State of Florida, in: Forensic Engineering 2018: Forging
627 Forensic Frontiers. American Society of Civil Engineers Reston, VA, pp.
628 1028–1038.
- 629 Powell, M.D., Houston, S.H., Amat, L.R., Morisseau-Leroy, N., 1998. The
630 HRD real-time hurricane wind analysis system. Journal of Wind Engineering
631 and Industrial Aerodynamics 77, 53–64.
- 632 Powell, M.D., Vickery, P.J., Reinhold, T.A., 2003. Reduced drag coefficient
633 for high wind speeds in tropical cyclones. Nature 422, 279–283.
- 634 Röhrs, J., Christensen, K.H., Hole, L.R., Broström, G., Drivdal, M., Sundby,
635 S., 2012. Observation-based evaluation of surface wave effects on currents
636 and trajectory forecasts. Ocean Dynamics 62, 1519–1533.
- 637 Schott, F.A., Lee, T.N., Zantopp, R., 1988. Variability of structure and
638 transport of the Florida Current in the period range of days to seasonal.
639 Journal of Physical Oceanography 18, 1209–1230.
- 640 Siadatmousavi, S.M., Jose, F., Stone, G., 2011. Evaluation of two WAM
641 white capping parameterizations using parallel unstructured SWAN with
642 application to the Northern Gulf of Mexico, USA. Applied Ocean Research
643 33, 23–30.
- 644 Sikirić, M.D., Roland, A., Janeković, I., Tomazić, I., Kuzmić, M., 2013.
645 Coupling of the Regional Ocean Modeling System (ROMS) and Wind
646 Wave Model. Ocean Modelling 72, 59–73.
- 647 Smith, N.P., 1982. Response of Florida Atlantic shelf waters to hurricane
648 David. Journal of Geophysical Research: Oceans 87, 2007–2016.
- 649 Stokes, G.G., 1880. On the theory of oscillatory waves. Transactions of the
650 Cambridge Philosophical Society .

- 651 Tolman, H.L., et al., 2009. User manual and system documentation of
652 WAVEWATCH III TM version 3.14. Technical note, MMAB Contribution
653 276, 220.
- 654 Van Den Bremer, T., Breivik, Ø., 2018. Stokes drift. Philosophical Trans-
655 actions of the Royal Society A: Mathematical, Physical and Engineering
656 Sciences 376, 20170104.
- 657 Villas Bôas, A.B., Cornuelle, B.D., Mazloff, M.R., Gille, S.T., Ardhuin, F.,
658 2020. Wave-current interactions at meso-and submesoscales: Insights from
659 idealized numerical simulations. Journal of Physical Oceanography 50,
660 3483–3500.
- 661 Wachnicka, A., Browder, J., Jackson, T., Louda, W., Kelble, C., Abdelrahman,
662 O., Stabenau, E., Avila, C., 2019. Hurricane Irmas impact on water quality
663 and phytoplankton communities in Biscayne Bay (Florida, USA). Estuaries
664 and Coasts , 1–18.
- 665 Weisberg, R., Liu, Y., Mayer, D., 2009. Mean circulation on the west Florida
666 continental shelf observed with long-term moorings. Geophys. Res. Lett
667 36, L19610.
- 668 Weisberg, R.H., Zheng, L., 2006. Hurricane storm surge simulations for
669 Tampa Bay. Estuaries and Coasts 29, 899–913.
- 670 Wu, L., Chen, C., Guo, P., Shi, M., Qi, J., Ge, J., 2011. A FVCOM-
671 based unstructured grid wave, current, sediment transport model, I. Model
672 description and validation. Journal of Ocean University of China 10, 1–8.
- 673 Xian, S., Feng, K., Lin, N., Marsooli, R., Chavas, D., Chen, J., Hatzikyriakou,
674 A., 2018. Brief communication: Rapid assessment of damaged residential
675 buildings in the Florida Keys after Hurricane Irma. Natural Hazards and
676 Earth System Sciences 18, 2041–2045.

- 677 Zedler, S., Niiler, P., Stammer, D., Terrill, E., Morzel, J., 2009. Ocean's
678 response to Hurricane Frances and its implications for drag coefficient
679 parameterization at high wind speeds. *Journal of Geophysical Research: Oceans* 114.
- 681 Zhang, C., Durgan, S.D., Lagomasino, D., 2019. Modeling risk of mangroves
682 to tropical cyclones: A case study of Hurricane Irma. *Estuarine, Coastal
683 and Shelf Science* 224, 108–116.